Suction-Side Gill Region Film Cooling: Effects of Hole Shape and Orientation on Adiabatic Effectiveness and Heat Transfer Coefficient

Justin Chappell
Department of Mechanical Engineering,
University of Utah,
50 S. Central Campus Drive,
MEB 2110,
Salt Lake City, UT 84112-9208

Phil Ligrani[1]
Donald Schultz Professor of Turbomachinery,
University of Oxford,
17 Foundry House,
Walton Well Road,
Oxford OX2 6AQ, England
e-mail: p_ligrani@msn.com

Sri Sreekanth
Principal Analyst
Pratt and Whitney Canada,
1801 Courtney Park Drive East,
Mississauga, ON, L5A 3S8, Canada
e-mail: sri.sreekanth@pwc.ca

Terry Lucas
Chief, Turbine Cooling and Static Structures
Pratt and Whitney Canada,
1000 Marie-Victorin, Longueuil,
QC, J4G 1A1, Canada
e-mail: terrance.lucas@pwc.ca

The performance of suction-side gill region film cooling is investigated using the University of Utah transonic wind tunnel and a simulated turbine vane in a two-dimensional cascade. The effects of film cooling hole orientation, shape, and number of rows, and their resulting effects on thermal film cooling characteristics, are considered for four different hole configurations: round axial (RA), shaped axial (SA), round radial (RR), and round compound (RC). The mainstream Reynolds number based on axial chord is 500,000, the exit Mach number is 0.35, and the tests are conducted using the first row of holes only, second row of holes only, or both rows of holes at blowing ratios of 0.6 and 1.2. Carbon dioxide is used as the injectant to achieve density ratios of 1.73 to 1.92 similar to values present in operating gas turbine engines. A mesh grid is used to give a magnitude of longitudinal turbulence intensity of 5.7% at the inlet of the test section. Results show that the best overall protection over the widest range of blowing ratios and streamwise locations is provided by either the RC holes or the RR holes. This result is particularly significant because the RR hole arrangement, which has lower manufacturing costs compared with the RC and SA arrangements, produces better or equivalent levels of performance in terms of magnitudes of adiabatic film cooling effectiveness and heat transfer coefficient. Such improved performance (relative to RA and SA holes) is most likely a result of compound angles, which increases lateral spreading. As such, the present results indicate that compound angles appear to be more effective than hole shaping in improving thermal protection relative to that given by RA holes.
[DOI: 10.1115/1.3151600]

1 Introduction

Researchers, manufacturers, and designers of turbine components in gas turbine engines have devoted much attention to the thermal performance of shaped film cooling holes and cylindrical holes with a variety of orientations in recent years. This is due to the fact that these holes often provide higher levels of thermal protection compared with round cylindrical shaped holes, which are oriented with simple angles in streamwise-normal planes. The resulting improved thermal protection is important because it leads to increases in engine performance and efficiency by allowing higher inlet temperatures. If component surface temperatures are also maintained at acceptable levels, increased part life is another benefit, provided associated high temperature effects, such as high-temperature oxidation, creep, corrosion, and thermomechanical fatigue, are minimized. Also important is the manufacturability of such holes, which requires minimum assembly costs without significant decreases in the level of thermal protection.

Recent investigations of the thermal performance of shaped holes consider a variety of film hole geometries, including conical-diffused holes [1,2], diffused trapezoidal shaped holes [3], square holes [4], shaped-inclined slots [5], forward-diffused holes [6–14], laterally diffused (or fan shaped) holes [7–9,11,14–19], and forward laterally diffused (or laid-back fan-shaped) holes [12,15–24]. A number of these studies consider shaped holes oriented with compound angle orientations [2,6,9,10,14,18,22,24]. Several of these consider shaped film hole geometries with simulated turbine airfoil geometry [18,19,23], high Mach number flow conditions along a flat plate [17], or simulated turbine airfoil geometry in high Mach number flows [24].

Of these investigations, Reiss and Bolcs [18] investigate cylinder leading edge film cooling from fan-shaped holes and laid-back fan-shaped holes with compound angle orientations. Teng and Han [19] and Brandt et al. [23] consider film cooling on turbine airfoil suction surfaces with laid-back-fan-shaped holes with simple angle orientations. The experimental study by Gritsch et al. [17] is conducted with high subsonic and supersonic Mach numbers, which approximate the conditions that exist in operating engines with transonic turbine components. Results show that higher effectiveness values are generally produced by holes with laid-back fan shapes (and simple angle orientations) than by cylindrical holes and fan-shaped holes (both also with simple angle orientations). Furukawa and Ligrani [24] consider the performance of cylindrical holes with simple angle orientations, laid-back fan-shaped holes with simple angle orientations, and laid-back fan-shaped holes with compound angle orientations. A symmetric airfoil with the Mach numbers ranging from 0.4 to 1.24 is employed. Results show that the highest local and spatially averaged film cooling effectiveness magnitudes are generally obtained with laid-back fan-shaped holes oriented with compound angles.

The present study considers the effects of film cooling hole shape, orientation, blowing ratio, as well as the number of rows of

[1]Corresponding author.

Contributed by the International Gas Turbine Institute of ASME for publication in the JOURNAL OF TURBOMACHINERY. Manuscript received February 12, 2009; final manuscript received February 26, 2009; published online April 7, 2010. Review conducted by David Wisler. Paper presented at the ASME Turbo Expo 2008: Land, Sea, and Air (GT2006), Berlin, Germany, June 9–13, 2008.

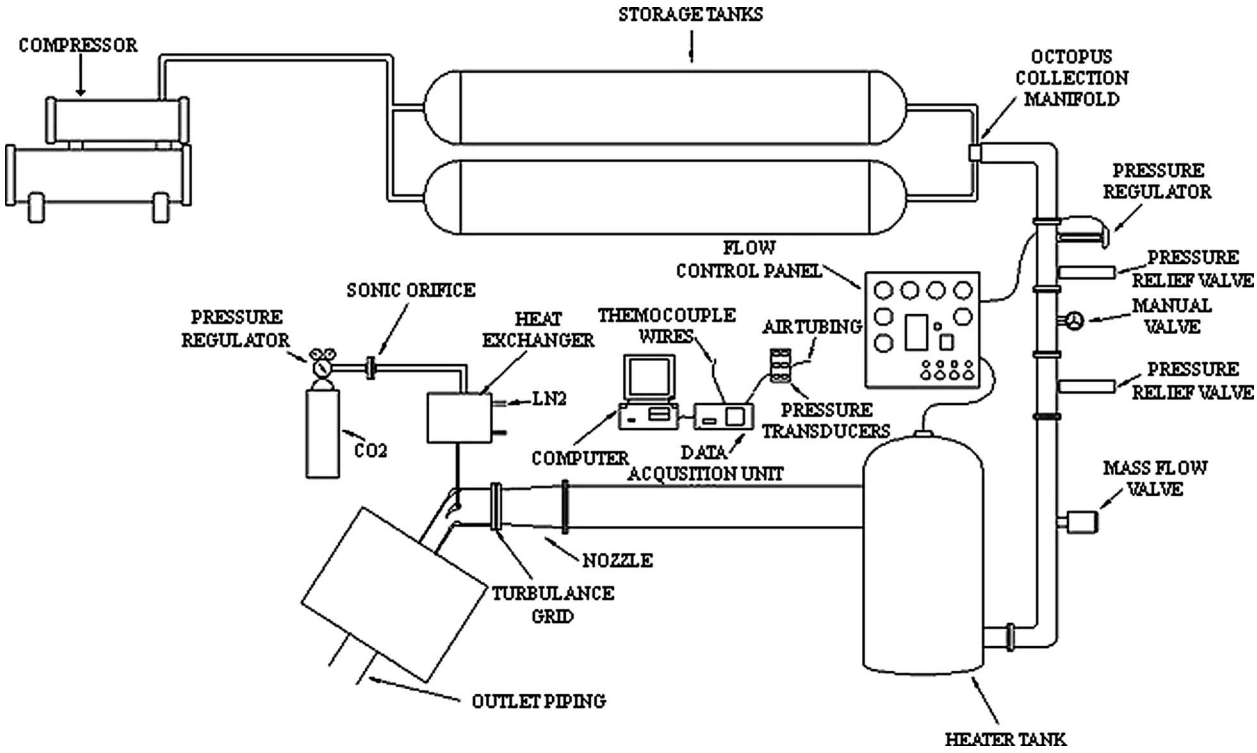

Fig. 1 University of Utah transonic wind tunnel

holes on surface distributions of adiabatic film cooling effectiveness and heat transfer coefficient in a high-speed compressible flow. The film cooling holes are located on the suction-side gill region of a simulated cambered turbine blade. Four different hole configurations are tested at two different blowing ratios, utilizing either a single row of holes at two different locations or two rows of film cooling holes. Carbon dioxide is used as the injectant to achieve density ratios of 1.73–1.92 similar to values present in operating gas turbine engines. A mesh grid is used to augment the magnitudes of longitudinal turbulence intensity at the inlet of the test section. As such, new film cooling data are provided beyond that provided by earlier investigators. This is due to that fact that the particular round radial (RR) and round compound (RC) arrangements investigated are new, and airfoil geometry, flow conditions, freestream pressure gradient, and boundary layer development simulate engine operating conditions. The present data thus provide useful information to designers of turbomachinery components and to individuals developing models for computational fluid dynamics (CFD) predictions of the thermal protection provided by different film cooling configurations. Corresponding aerodynamic data for similar experimental conditions and configurations are given in a companion paper [25].

2 Experimental Apparatus and Procedures

2.1 Transonic Wind Tunnel. The University of Utah transonic wind tunnel (TWT) is used for the study and is shown schematically in Fig. 1. The TWT blow-down type facility consists of two main parts: (i) compressor and storage tanks and (ii) wind tunnel. The wind tunnel consists of five major subsections: (i) flow rate and pressure level management apparatus, (ii) plenum tank, (iii) inlet ducting and test section, (iv) plenum, exit ducting, and ejector, and (v) control panel. Detailed descriptions are provided by Ligrani and co-workers [24,26,27].

A compressor from Gardner Denver Co. is used to pressurize the array of eight tanks whose total capacity volume is 11.9 m^3. A desiccant dryer, an oil filter, and two particulate filters are located just downstream of the compressor to remove particulates and moisture from the air. A Fisher pressure regulator with a sliding gate valve, a Fisher diaphragm actuator, a valve positioner, and a process controller are used to regulate the pressure in the test section as the storage tanks discharge. A plenum tank, a 30.48 cm inner diameter pipe, a circular-to-square transition duct, a nozzle, and the test section then follow. Relative humidity at the test section inlet is typically 20–30%. The test section is connected to a large $92.71 \times 91.44 \times 1.44$ cm^3 plenum with a square plastic flange at its outlet. The plenum diffuses high speed air from the test section exit into a reservoir of low velocity air. This plenum is then connected to two ducts, which are subsequently connected to the atmosphere.

2.2 Test Section and Test Vane. The present test section is designed to match the Reynolds numbers, Mach numbers, pressure gradients, passage mass flow rates, boundary layer development, streamline curvature, airfoil camber, and physical dimensions of turbine vanes in operating aero-engines and in gas turbines used for utility power generation. A schematic diagram of the test section with the cambered vane is shown in Fig. 2. The inlet of the test section is 12.70×12.70 cm^2. The side and bottom walls of the test section are made of steel and the top wall is made

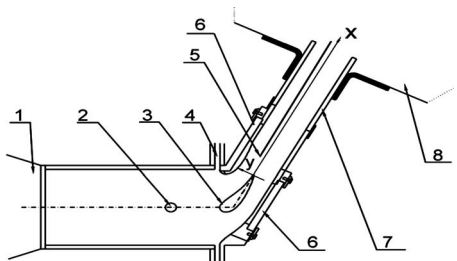

Fig. 2 Schematic diagram of the test section

Table 1 Film cooling experimental configurations and conditions

Hole configuration	m	Density ratio		
		FR	SR	BR
Round axial	0.6	1.82	1.73	1.81
Round axial	0.9	1.82	1.84	1.88
Round axial	1.2	1.92	1.86	1.84
Round radial	0.6	1.75	1.79	1.84
Round radial	0.9	1.84	1.83	1.77
Round radial	1.2	1.92	1.86	1.9
Shaped axial	0.6	1.82	1.73	1.81
Shaped axial	0.9	1.82	1.84	1.86
Shaped axial	1.2	1.92	1.86	1.84
Round compound	0.6			1.8
Round compound	0.9			1.83
Round compound	1.2			1.87

up of acrylic. As shown in Fig. 2, two zinc-selenide windows can be placed on both of the side walls so that the entire airfoil surface is accessible to optical surface temperature measurement schemes such as infrared thermography.

Appropriate cascade flow conditions are maintained, in part, by a pair of adjustable bleed ducts, which are located on the two side walls, as shown in Fig. 2. The flow rate of each bleed duct is regulated using an adjustable ball valve. Following these, the test section walls have the same pressure-side and suction-side contours as the test vane. The exit area and exit flow direction from the cascade test section can be altered by changing the angles of the two exit tailboards, which are also shown in Fig. 2. Thus, (i) changing the total pressure at the test section inlet using the pressure regulator/sliding gate valve arrangement, (ii) changing the angular positions of the two tailboards, and (iii) adjusting the ball valves of the bleeding system are employed to alter the Mach number distribution along the vane in the test section for a particular vane and test section configuration. By adjusting these items, appropriate Mach number distributions along the test vane are obtained.

Experimental film cooling configurations and conditions employed in the present study are tabulated in Table 1. Here, FR, SR, and BR refer to first row of holes only, second row of holes only, and both rows of holes, respectively. Table 2 gives geometric parameters of the test vane. The coordinates of this test vane profile were provided by the personnel of Pratt and Whitney Canada Corporation, along with the flow conditions present in the associated operating environment.

2.3 Film Cooling Hole Configurations. The four different hole configurations, which are investigated, are shown in Fig. 3: round axial (RA), shaped axial (SA), round radial (RR), and round compound (RC). For each configuration, either the first upstream row of holes only is employed, the second row of holes only is employed, or two rows of holes are employed. With this last arrangement, the holes located in each row are staggered with respect to each other. A different vane is used for each different hole arrangement (first row, second row, and both rows) and for each hole configuration (RA, SA, RR, and RC). Thus, a total of 12 vanes are employed overall. As shown in Fig. 4, the hole exits for all four arrangements are located at 15% and 25% of the axial chord. In addition, the holes in each row have the same spanwise hole diameter spacing of $6d$. The row of holes marked A-A in Fig. 3 contains 13 film cooling holes, and the row of holes marked B-B in Fig. 3 contains 14 film cooling holes. Note that the RR and RC configurations are unique because of the large compound angles, which are employed.

Table 2 Test vane geometric parameters

Parameter	Unit	Value
True chord C	cm	7.27
Axial chord C_x	cm	4.85
Pitch p	cm	6.35
Span	cm	12.7
Flow turning angle	deg	62.75

2.4 Secondary Film Coolant Injection System. Carbon dioxide is used as the injectant to achieve density ratios similar to those experienced in operating gas turbine engines $\rho_c/\rho_\infty = 1.73-1.92$. With the present secondary injection system arrangement, regulated carbon dioxide leaves its tank and first goes through a sonic orifice, which is used in conjunction with pressure and temperature measurements to determine the injectant mass flow rate. After leaving the sonic orifice, the injectant enters a TV-050 heat exchanger (also shown in Fig. 1), which uses liquid nitrogen as a coolant. As the injectant is cooled, it is passed through bypass valves until the mainstream air is started, to prevent any advance cooling of the vane. Just prior to the mainstream blow down, valves are arranged so that the injectant flows through the vane and out of the film cooling holes. To approximate a plenum condition, the injectant enters the injectant passage from both the top and bottom of the vane.

2.5 Pressure and Temperature Measurements. As tests are conducted, Validyne model DP15-46 pressure transducers (with diaphragms rated at either 34.5 kPa or 344.7 kPa), and calibrated copper-constantan thermocouples are used to sense pressures and temperatures at different locations throughout the facility. Signals from the pressure transducers are processed by Celesco model CD10D carrier demodulators. All pressure transducer measurement circuits are calibrated using a Wallace and Tiernan FA145 bourdon tube pressure gage as a standard. A United Sensor PLC-8-KL pitot-static probe with an attached, calibrated Watlow standard type-K copper-Constantan thermocouple, and a four-hole conical-tipped pressure probe also with a similar Watlow thermocouple are used to sense total pressure, static pressure, and recovery temperature at the inlet and exit of the test section, respectively, during each blow down. Mach numbers, sonic velocities, total temperatures, and static temperatures are determined from these data. The four-hole probe has a tip, which is 1.27 mm in diameter, and a stem, which is 3.18 mm in diameter. Each port has a diameter of 0.25 mm. The overall response time of the pressure measuring system is about 0.2 s. The conical probe is aligned using two yaw ports placed on either side of the probe. The probe is located downstream of the vane. The position in the streamwise direction is adjustable.

Voltages from the carrier demodulators and thermocouples are read sequentially using Hewlett-Packard HP44222T and HP44222A relay multiplexer card assemblies, installed in a Hewlett-Packard HP3497A low-speed data acquisition/control unit. This system provides thermocouple compensation electronically such that voltages for type-T thermocouples are given relative to 0°C. The voltage outputs from this unit are acquired by the Dell Precision PC workstation through its USB port, using LABVIEW 7.0 software and a GPIB-USB-B adaptor made by National Instruments.

2.6 Mainstream Flow Turbulence Level. A fine mesh grid arrangement is used at the inlet of the test section to augment the magnitude of mainstream turbulence intensity [28]. The fine mesh grid consists of an array of four square rods arranged horizontally and four square rods arranged vertically. Each rod is spaced 25.4 mm from the adjacent rods and is 5 mm on each side. The open area amounts to 48% of the inlet area. The installation position for the fine mesh grid is at the exit of the nozzle, as shown in Fig. 2.

2.7 Longitudinal Turbulence Intensity Measurements. A single horizontal-type platinum-plated tungsten hot-wire sensor,

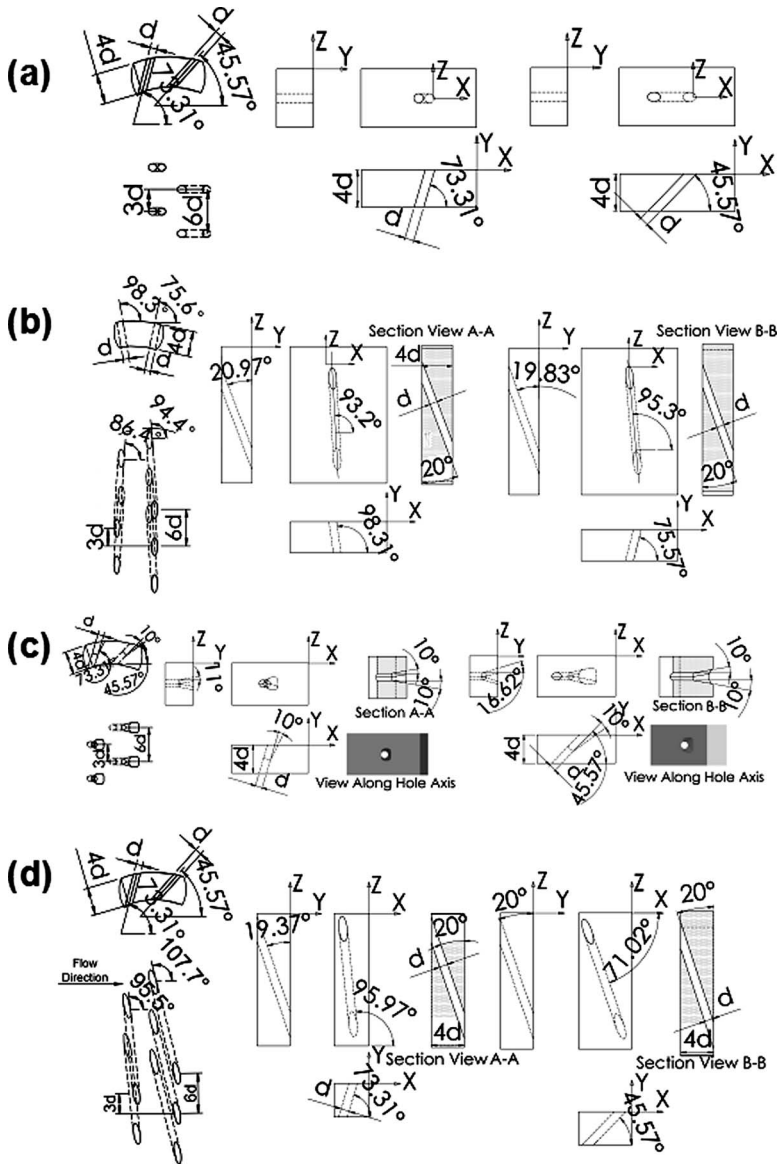

Fig. 3 Film cooling hole configurations: (*a*) RA, (*b*) RR, (*c*) SA, and (*d*) RC

with a diameter of 12.7 μm and a length of 2.54 mm, is employed to measure the time-varying longitudinal component of velocity at the inlet of the test section. The time-averaged longitudinal velocity and the longitudinal turbulence intensity are then determined from these measurements. The measurement location is one axial chord length upstream of the vane leading edge. The hot-wire probe is driven by a Disa 55M10 constant-temperature hot-wire anemometer bridge with an overheat ratio of 1.6. The analog signal from this bridge is then processed using a Dantec 56N20 signal conditioner with a low-pass anti-aliasing filter set to 100 kHz. The time-varying output voltage signal is then sampled at a 200 kHz rate using a Datel PCI441D I/O board installed in the Dell Precision 530 PC workstation. During each measurement, 2×10^6 voltage values are sampled over a time period of 10 s. Data are acquired using LABVIEW 7.0 software and then processed further using MATLAB 6.1 software. The entire measurement system, including the hot-wire sensor, is calibrated in the freestream of the TWT. A Kiel type pressure probe, wall static taps, and a copper-Constantan thermocouple are used to measure and determine the total pressure, static pressure, recovery temperature, and velocity at the inlet of the test section as the calibration is conducted.

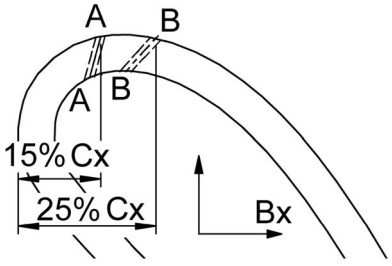

Fig. 4 Film cooling hole locations

2.8 Local Adiabatic Film Cooling Effectiveness and Heat Transfer Coefficient Measurements. Coolant stagnation temperature is determined from measurement of the coolant recovery temperature just upstream of the coolant plenum using a calibrated copper-Constantan thermocouple. Knowing the Mach number in this passage, the coolant stagnation temperature is then determined, after the measured temperature is corrected for time

lag errors due to the finite size of the thermocouple junction. All adiabatic effectiveness and heat transfer coefficient experiments are repeated twice to verify the consistency and repeatability of the results.

Spatially resolved temperature distributions along the airfoil surface are determined using infrared imaging in conjunction with thermocouples, energy balances, digital image processing, and in situ calibration procedures. To accomplish this, the infrared radiation emitted by the epoxy surfaces of the airfoil is captured using an inframetrics infrared imaging camera, which operates at infrared wavelengths from 8 μm to 14 μm. Temperatures, measured using calibrated copper-Constantan thermocouples distributed along the surface adjacent to the flow, are used to perform the in situ calibrations simultaneously as the radiation contours from surface temperature variations are recorded.

This is accomplished as the camera views the suction test surface through a custom made cylindrical zinc-selenide window (which transmits infrared wavelengths between 6 μm and 17 μm). Reflection and radiation from surrounding laboratory sources are minimized using opaque shields, which cover the camera lens and the zinc-selenide window. Twelve to fifteen thermocouple junction locations are present in any field viewed by the camera. The exact spatial locations and pixel locations of these thermocouple junctions and the coordinates of a 5×5 cm^2 field of view are determined from calibration maps obtained prior to measurements. During this procedure, the camera is focused and rigidly mounted and oriented relative to the test surface in the same way as when radiation contours are recorded.

With these data, gray scale values at pixel locations within video taped images from the infrared imaging camera are readily converted to temperatures. Because such calibration data depend strongly on camera adjustment, the same brightness, contrast, and aperture camera settings are used to obtain the experimental data. The in situ calibration approach rigorously and accurately accounts for these variations.

The camera is calibrated by first adjusting for the zinc-selenide window's transmissivity by changing the blade temperature and measuring a location on the surface of the blade without the window in place, and then measuring the same location with the window in place, adjusting the camera's transmissivity value until they were the same. The resulting transmissivity of the zinc-selenide window is 0.98. A similar procedure is used to adjust the camera for the blade material emissivity. To accomplish this, a thermocouple is placed on the blade surface and the camera is set to measure the same location as the thermocouple. The temperature of the blade is changed and the emissivity value is adjusted until the IR camera and thermocouple measured the same values. As this is done, radiation exchange between the test section walls and blade surface are assumed to be negligible.

Images from the infrared camera are recorded as 8 bit gray scale directly into the memory of a Dell Dimension XPS T800r PC using a Scion image corporation frame grabber video card, and SCION IMAGE v.1.9.2 software. Three sets of 60 frames are recorded at a rate of one frame per second. This is done about 12.0 s. after each blow down begins because the film and freestream flows are established, and to obtain data when the test surface approximates an adiabatic surface condition. All of 180 resulting images are then ensemble averaged to obtain the final gray scale data image. This final data set is then imported into MATLAB version 6.0.0.88 (Release 12) software to convert each of the 256 possible gray scale values to local temperature and then into local effectiveness at each pixel location using calibration data. Each resulting individual image then covers a 300 pixel$\times$300 pixel area.

For the adiabatic surface measurements, as well as for the surface heat transfer coefficient measurements, the airfoils are epoxy. Variations in surface temperature are then related to variations in surface adiabatic film cooling effectiveness, surface Nusselt number, and surface heat transfer coefficients.

2.9 Local Surface Adiabatic Film Cooling Effectiveness Distributions. The local adiabatic film cooling effectiveness is given by $\eta=(T_{\text{ad}}-T_\infty)/(T_{oc}-T_\infty)$. This is measured from simultaneous direct measurement of T_∞ and T_{oc}, as well as airfoil surface distributions of T_{ad}. These quantities are determined at equilibrium conditions, which are established during blow-down testing. Surface T_{ad} distributions are determined from infrared thermography measurement of surface airfoil temperature distributions. These approximate adiabatic surface temperatures because of the relatively low thermal conductivity of the epoxy airfoils employed ($k=0.02$ W/m K).

2.10 Analysis Procedures to Determine Local Surface Heat Transfer Coefficients. With the airfoil surface initially in thermal equilibrium at temperature $T_\infty=T_{oc}=T_i$ (where T_∞ is the crossflow mainstream recovery temperature, T_{oc} is the jet stagnation temperature, and T_i is the initial surface temperature), transient one-dimensional heat conduction occurs when a sudden change in temperature is imposed on the jet flow. The 1D semi-infinite solid formulation is then a convenient approach. At any time during the transient and at any particular location on the surface of interest, the following expression relates the film heat transfer coefficient h_f and the adiabatic wall temperature T_{ad} with the initial temperature T_i, the temperature of the surface T_w, and physical properties of the wall material α.

$$\frac{(T_w(t)-T_i)}{(T_{\text{ad}}-T_i)}=1-\exp(h_f^2\alpha t/k^2)\text{erfc}(h_f\sqrt{\alpha t}/k) \tag{1}$$

The initial and boundary conditions for Eq. (1) are then given by

$$T(z,t=0)=T_i \tag{2}$$

$$T(z=\infty,t)=T_i \tag{3}$$

$$-k\left(\frac{\partial T}{\partial z}\right)_{z=0}=h_f(T_{\text{ad}}-T_w(t)) \tag{4}$$

where z is the coordinate that is perpendicular to the blade surface. Equation (1) is adapted from Carslaw and Jaeger [29] from the solution to the one-dimensional transient heat conduction into a semi-infinite wall with the initial and boundary conditions specified by Eqs. (2)–(4). The film heat transfer coefficient h_f is then defined using an expression of the form

$$h_f=q_w/(T_w-T_{\text{ad}}) \tag{5}$$

where q_w is the heat flux at the wall, T_w is the measured temperature of the wall, and T_{ad} is the adiabatic temperature of the wall or the temperature achieved at the wall when $q_w=0$.

In a film cooling application, the adiabatic wall temperature is unknown and is a function of the location on the surface, crossflow, jet flow temperatures, and the degree of mixing between them. For each location on the surface, Eq. (1) has therefore two unknowns, h_f and T_{ad}. The latter can be defined by the use of the film cooling effectiveness, which is given by

$$\eta=(T_{\text{ad}}-T_\infty)/(T_{oc}-T_\infty) \tag{6}$$

so that the denominator in the left hand side of Eq. (1) is then of the form expressed using

$$T_{\text{ad}}-T_i=\eta(T_{oc}-T_\infty)+(T_\infty-T_i) \tag{7}$$

The unknowns conveniently become h_f and η. The experiment has to produce only the value of the surface temperature during the transient $T_w(t)$ at all desired locations on the surface of interest. Two equations in the form of Eq. (1) can be written for each point on the surface and at different times during the transient $t=t_a$ and $t=t_b$, to provide the two needed relationships for the simultaneous calculation of h_f and η at that location.

Theoretically, any two time events can be chosen from the transient history during one test, or two separate tests can be conducted with the same flow field but different flow temperatures to

calculate a time-independent heat transfer coefficient and film cooling effectiveness. The latter technique has been used in the past in film cooling applications and can be categorized as a double sampling or double event procedure. A double event procedure provides the minimum required information for calculating h_f and η in a three-temperature situation, while a single event procedure provides all the necessary information for calculation of the heat transfer coefficient in a two-temperature situation.

In typical jets in crossflow applications, unsteady vortex structures are often observed downstream of the injection sites. In such situations, the double sampling techniques, as used in the past, may not lead to an accurate representation of the heat transfer characteristics. Multiple sampling provides further information in these cases and locally time averaged h_f and η provide higher accuracy in the representation of the heat transfer process on the surface of interest. Even in a perfectly steady flow field, the multiple sampling technique improves the accuracy by noise minimization through the time-averaging procedure. The term noise is used here to describe random errors in temperature measurement. In the present study, a multiple sampling technique is used with the advantage that η and h_f are calculated simultaneously during a single transient test.

A true step change in the temperature of the jet flow could not be achieved in the experiments, so that the temperature of the jets is actually a function of time $T_{oc}=T_{oc}(t)$. This information is incorporated in the solution to the transient heat transfer problem described by Eq. (1), by a method similar to that described by Metzger and Larson [30], where the actual temperature rise is obtained from a superimposed set of incremental steps. For any arbitrary time event pair $t=t_a$ and $t=t_b$, a nonlinear equation for the unknown variable h_f can be written in the form given by

$$\frac{T_w(t_a)-T_\infty}{T_w(t_b)-T_\infty} = \frac{\sum_{i=1}^{N_a}\left\{1-\exp\left(\frac{h_f^2(t_a-\tau_i)}{\rho ck}\right)\mathrm{erfc}\left(\frac{h_f\sqrt{t_a-\tau_i}}{\sqrt{\rho ck}}\right)\right\}(\Delta T_2)_i}{\sum_{i=1}^{N_b}\left\{1-\exp\left(\frac{h_f^2(t_b-\tau_i)}{\rho ck}\right)\mathrm{erfc}\left(\frac{h_f\sqrt{t_b-\tau_i}}{\sqrt{\rho ck}}\right)\right\}(\Delta T_2)_i} \tag{8}$$

where $(\Delta T_{oc})_i=(\Delta T_2)_i$, which are the finite jet temperature changes corresponding to the discretized time events N_a for $t=t_a$ and N_b for $t=t_b$. Film cooling effectiveness can be thus calculated from the wall temperature response at either time event, $t=t_a$ or $t=t_b$. For example,

$$\eta = \frac{T_w(t_a)-T_\infty}{\sum_{i=1}^{N_a}\left\{1-\exp\left(\frac{h_f^2(t_a-\tau_i)}{\rho ck}\right)\mathrm{erfc}\left(\frac{h_f\sqrt{t_a-\tau_i}}{\sqrt{\rho ck}}\right)\right\}(\Delta T_2)_i} \tag{9}$$

Equations (8) and (9) are solved numerically for a series of time event pairs. The time-dependent history of η and h_f are then obtained, and the mean values are calculated by averaging through a chosen time interval. In the present investigation, only h_f values are determined using this procedure.

2.11 Experimental Uncertainties. Uncertainty estimates are based on 95% confidence levels and determined using procedures described by Kline and McClintock [31] and by Moffat [32]. The Mach number uncertainty is 0.002. The uncertainty of temperatures is $\pm 0.15\,^\circ$C. The pressure uncertainty is ± 0.25 kPa. The spatial and temperature resolutions achieved with the infrared imaging are about 0.05 mm and $0.8\,^\circ$C, respectively. This magnitude of temperature resolution is due to uncertainty in determining the exact locations of thermocouples with respect to pixel values used for the in situ calibrations. Local adiabatic film effectiveness uncertainty is then about ± 0.015% or about ± 6.0% for a nominal effectiveness value of 0.25. These local effectiveness uncertainty values are slightly higher within about 1.0 hole diameter of the hole exits due to some three-dimensional effects within the epoxy in the vicinity of the holes. Experimental uncertainty magnitudes of spanwise-averaged heat transfer coefficients are ± 7–10% or approximately ± 12 W/m^2 K for a spanwise-averaged heat transfer coefficient value of 150 W/m^2 K.

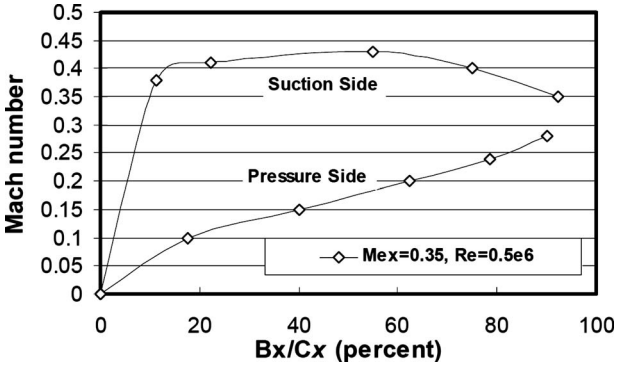

Fig. 5 Vane Mach number distribution

3 Experimental Results

3.1 Test Section Flow Characteristics and Mach Number Distributions. During each blow-down test, the total pressure, Reynolds number, and turbulence level at the test section inlet are maintained in a continuous and steady fashion for up to 45 s long time intervals, as detailed by Jackson et al. [27]. Such characteristics are not only a result of TWT design but also the excellent performance of the TWT mainstream air pressure regulator and its controller. During each test, the inlet total pressure at the inlet of the test section (one axial chord length upstream of the vane leading edge) is maintained constant at 94 kPa. This corresponds to an exit freestream Mach number of 0.35 and an exit Reynolds number based on axial chord of 0.5×10^6, as measured 0.25 axial chord lengths downstream the airfoil trailing edge.

The magnitudes of the inlet mainstream longitudinal turbulence intensity and length scale for the present experimental conditions are 5.7% and 2.2 cm, respectively. Here, turbulence intensity is defined as the ratio of the root-mean-square of the longitudinal fluctuation velocity component divided by the local streamwise mean component of velocity. The autocorrelation function is integrated with respect to the time lag to obtain the longitudinal integral time scale, which is then multiplied by the mean velocity to get the longitudinal integral length scale, which is a representative of the largest eddies in the turbulent flow field.

Inlet uniformity measurements are conducted at five different pitchwise locations at the inlet of the test section. With no turbulence grid employed, the total pressure and static pressure show excellent spatial uniformity at this location, varying by less than 0.5% of mean values. With the fine mesh grid, the total pressure and static pressure generally vary less than 0.6% of mean values. Note that the fine mesh grid is installed some distance away from the leading edge of the vane to maintain an acceptable level of uniformity in the flow as it approaches the vane.

Figure 5 shows the Mach number distributions along the turbine vane pressure side and along the vane suction side for the present operating conditions. The data shown in this figure are based on measurements of total pressure at the test section inlet and vane midspan static pressures. Compressible flow analysis in the form of isentropic relations is used to calculate Mach number distributions around the vane. These are measured using an airfoil that is constructed especially for this task. The vane has five pressure taps on the pressure side and five pressure taps on the suction side, as well as one pressure tap located on the leading edge at the

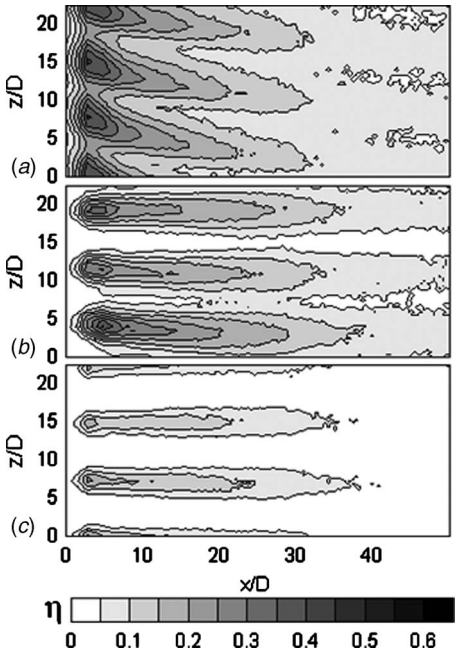

Fig. 6 Local adiabatic effectiveness distributions for $m=1.2$ for first row of holes only: (*a*) RR hole configuration, (*b*) SA hole configuration, and (*c*) RA hole configuration

vane midspan. As shown in Fig. 5, the Mach number distribution employed in this study is subsonic on the vane suction and pressure sides, with an adverse pressure gradient on the suction side of the vane when $Bx/c_x > 0.60$. As such, the present Mach number distribution is in excellent agreement with data for gas turbine vanes from industry [28].

3.2 Local Adiabatic Film Cooling Effectiveness Distributions. Spatially resolved plots of the local adiabatic film cooling effectiveness are presented in unrolled planar coordinates in

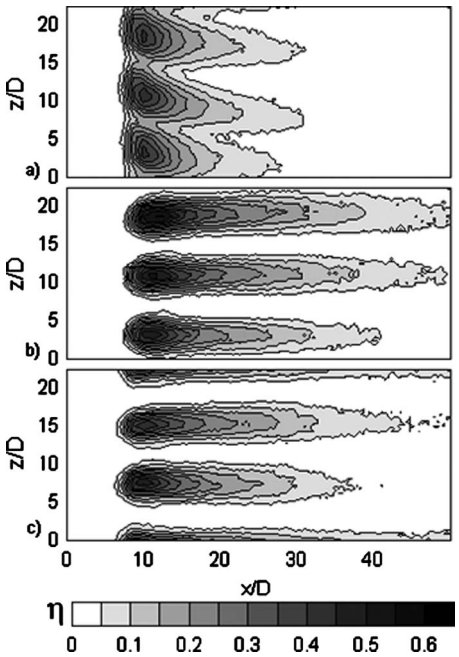

Fig. 7 Local adiabatic effectiveness distributions for $m=0.9$ for second row of holes only: (*a*) RR hole configuration, (*b*) SA hole configuration, and (*c*) RA hole configuration

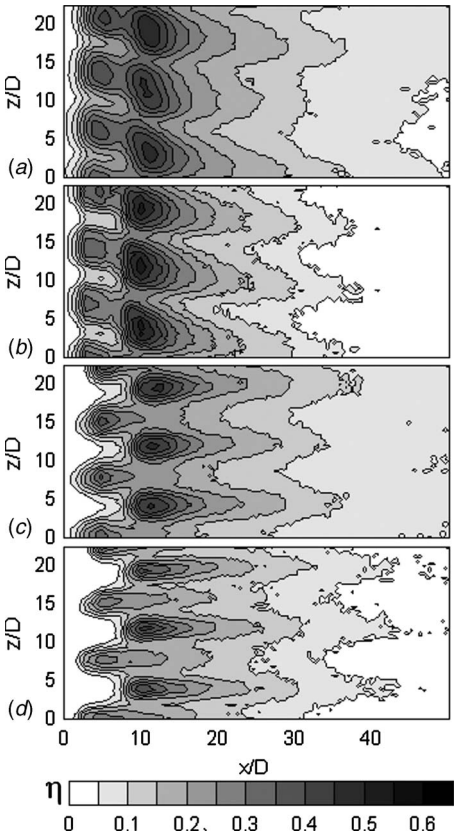

Fig. 8 Local adiabatic effectiveness distributions for $m=0.6$ for both rows of holes: (*a*) RC hole configuration, (*b*) RR hole configuration, (*c*) SA hole configuration, and (*d*) RA hole configuration

Figs. 6–8 for first row of holes only ($m=1.2$), second row of holes only ($m=0.9$), and both rows of holes ($m=0.6$), respectively. These local effectiveness data are given for all four hole configurations (RA, SA, RR, and RC). For comparison purposes, all of the plots utilize the same contour level values.

Figures 6 and 7 show that the RR configuration data are skewed with respect to the streamwise x/D direction because of radial hole orientations. This configuration also provides the highest local effectiveness values near and just downstream of the holes, with evidence of more uniform film coverage compared with distributions produced by the SA and RA arrangements. The highest local effectiveness values near and just downstream of the hole locations in Fig. 8 (for both rows of holes) are produced by the RC and RR configurations. These data thus provide evidence that compound angle orientations are more efficient than hole shaping in giving high values of film cooling effectiveness compared with RA holes (for the present arrangements and flow conditions). The use of a hole orientation also keeps larger concentrations of injectant near the blade surface and serves to increase the spanwise coverage of the injectant [14]. Note that the RR and RC hole configurations also produce very good streamwise film coverage, though depending on the hole location and blowing ratio, the other configurations may sometimes perform better. This is especially noticeable for the second row only configuration data, which are presented in Fig. 7.

The results in Figs. 6–8 also show that the RA configuration produces the lowest effectiveness values and most nonuniform film coverage. This is due to detachment of the coolant jets from the surface from the concentrated distributions of jet momentum produced by arrays of these holes. This effect is partially remedied

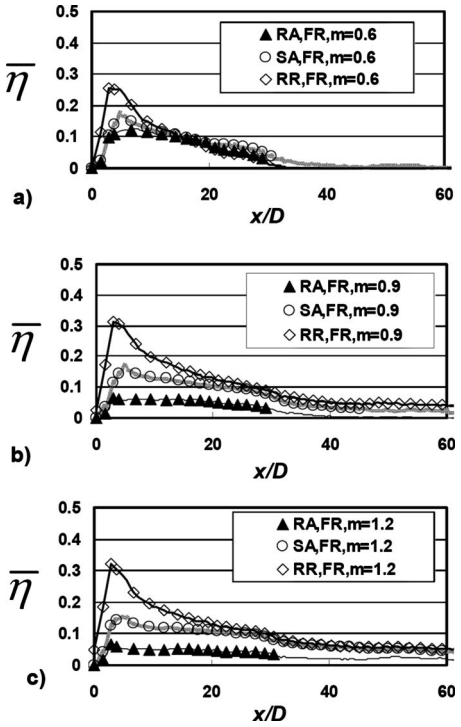

Fig. 9 Spanwise-averaged adiabatic film cooling effectiveness distributions for the first row of holes only: (*a*) *m*=0.6, (*b*) *m*=0.9, and (*c*) *m*=1.2

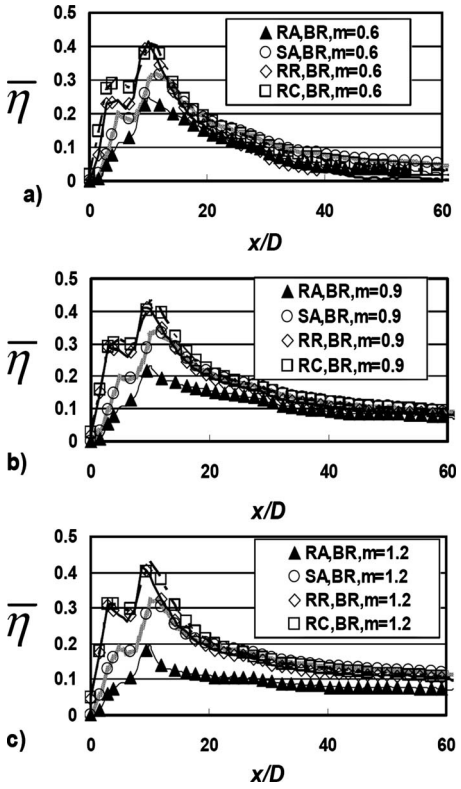

Fig. 11 Spanwise-averaged adiabatic film cooling effectiveness distributions for both rows of holes: (*a*) *m*=0.6, (*b*) *m*=0.9, and (*c*) *m*=1.2

by the diffusion effects of the SA holes, which decrease axial momentum magnitudes and increase injectant spreading. The result is higher local effectiveness values and improved surface film distributions for the SA hole data compared with the RA hole data given in Figs. 6–8.

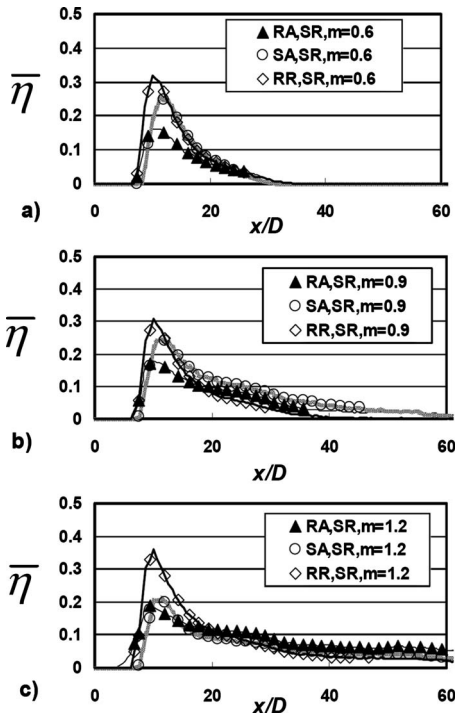

Fig. 10 Spanwise-averaged adiabatic film cooling effectiveness distributions for the second row of holes only: (*a*) *m*=0.6, (*b*) *m*=0.9, and (*c*) *m*=1.2

3.3 Spanwise-Averaged Adiabatic Film Cooling Effectiveness Distributions. Spanwise-averaged effectiveness values are determined by averaging local adiabatic effectiveness across three hole periods. The resulting spanwise-averaged results, which include comparisons of the different hole configurations, are presented in Figs. 9–11.

Figure 9 shows first row only data at blowing ratios of 0.6, 0.9, and 1.2. Here, the RR hole configuration generally gives the highest spanwise-averaged effectiveness values, especially near the film hole locations (including positions where local maxima are present). This particular configuration continues to maintain the highest spanwise-averaged effectiveness magnitudes up to $x/D=60$ when the blowing ratios are 0.9 and 1.2. This is due to the fact that larger concentrations of coolant are maintained at locations near the test surface as the film from RR holes is advected downstream. When data for different blowing ratios are compared, one important effect of increasing blowing ratio is then relative to downstream effectiveness values, since higher blowing ratios generally result in higher spanwise-averaged effectiveness values at $x/D>10-20$. Note also that, as the blowing ratio increases from 0.6 to 0.9, the peak effectiveness value for the RA configuration decreases, whereas the opposite is true for the RR configuration. These qualitative trends continue as the blowing ratio increase from 0.9 to 1.2; however, the quantitative changes appear to be somewhat less.

Shown in Fig. 10 are spanwise-averaged effectiveness values for the second row only arrangement. Compared with the first row only data, peak adiabatic effectiveness values are higher but are also more localized. Even though the second row of holes is located further downstream than the first row of holes; downstream effectiveness values for the second row only arrangement are often lower than the first row only configuration. A comparison of results in Figs. 9 and 10 shows that the RA configuration performs much better when it produces film from the second row location,

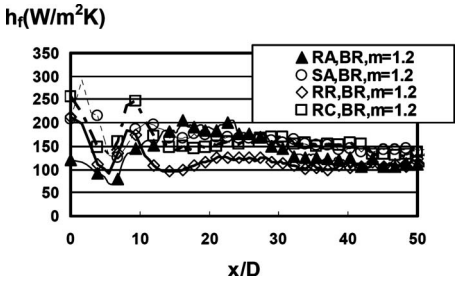

Fig. 12 Spanwise-averaged film cooling heat transfer coefficient distributions for both rows of holes arrangement for a blowing ratio *m* of 1.2

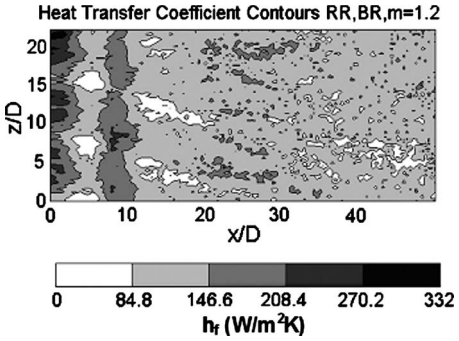

Fig. 13 Local film cooling heat transfer coefficient distribution for *m*=1.2 for the RR hole configuration and both rows of holes arrangement

and this is most noticeable at the two higher blowing ratios of 0.9 and 1.2 when $x/D<30$. As for the first row only configuration, Fig. 10 shows that increasing the blowing ratio m has important effects on downstream adiabatic effectiveness magnitudes. Also notice that spanwise-averaged data for the RR and RA configurations increase with blowing ratio for most values of x/D. In contrast, with the SA configuration, upstream effectiveness values decrease, whereas downstream effectiveness values increase as the blowing ratio becomes larger.

Like present results in Figs. 9 and 10, spanwise-averaged effectiveness data from Ref. [24] for a single row of holes are higher for shaped axial holes (in this case, laid-back fan-shaped holes) than for RA holes, especially for $x/D<10-20$. These authors also show that additional increases in spanwise-averaged effectiveness are present when the laid-back fan-shaped holes are arranged with compound angle orientations, especially for blowing ratios in the vicinity of 1.0.

Shown in Fig. 11 are comparisons of spanwise-averaged effectiveness values for the different hole configurations, when both rows of holes are employed. In all cases, effectiveness values peak near hole exits and then decrease. In many cases, double local maxima are apparent near hole locations, especially for the SA, RR, and RC configurations. Note that RC hole data are only given for the both rows of hole configuration. Comparisons of the different data in Fig. 11 show that the RC and the RR hole configurations give the overall best performance. When data in Figs. 9–11 are compared, both row configuration gives higher effectiveness values than either the first row only or the second row only configurations. Like the first and second row configurations, results in Fig. 11 show that changes in the blowing ratio mostly affect effectiveness values further downstream, and that differences in spanwise-averaged film effectiveness between the different configurations are most noticeable just downstream of the hole exits.

3.4 Spanwise-Averaged Film Cooling Heat Transfer Coefficient Distributions. Spanwise-averaged film cooling heat transfer coefficient values are also determined by averaging local values across three hole periods. Some examples of the resulting spanwise-averaged results, which include comparisons of the different hole configurations, are presented in Fig. 12 for a blowing ratio m of 1.2 and both rows of hole arrangement.

Here, the spanwise-averaged distribution for each film hole configuration shows significant variations just downstream of hole exits at $x/D<15$. For each hole configuration (RA, SA, RR, and RC), two separate peaks in heat transfer coefficient are present over this region. These are likely due to the variety of secondary flows and vortices, which accompany film development and often result in local augmentations of turbulent transport. Further downstream, the variation in heat transfer coefficient for each configuration is approximately constant with x/D. In general, the RR hole configuration produces the lowest h_f values in this region, and the RA hole configuration gives the highest.

3.5 Local Film Cooling Heat Transfer Coefficient Distributions. Two examples of local spatially resolved film cooling heat transfer coefficient distributions are presented in Figs. 13 and 14. These are given for the RR and RC hole configurations, respectively, for a blowing ratio m of 1.2 and both rows of hole arrangement. The distributions for these particular hole configurations are chosen for presentation because they generally give the best overall thermal protection in terms of the highest adiabatic film cooling effectiveness magnitudes and the lowest heat transfer coefficient magnitudes. In both cases, the most significant local heat transfer coefficient variations in Figs. 13 and 14 are present at $x/D<15$. Here, a variety of local deficits and maxima heat transfer coefficients are present, which are mostly a result of the placement of the different film cooling holes in the two staggered rows and the subsequent mixing and shear interactions that occur. Further downstream, the heat transfer coefficient distributions for the RR and RC configurations in Figs. 13 and 14 are more uniform, with only small variations with streamwise and spanwise locations. Brandt et al. [23] presented surface heat transfer coefficient distributions, which show double peaks just downstream of round axial holes. These are attributed to local flow separation regions, which form as the coolant is ejected from each individual hole. The extent and intensity of these separation zones appear to be less for laid-back fan-shaped holes since local heat transfer coefficient augmentations are spread uniformly just downstream of each hole exit.

4 Summary and Conclusions

The performance of suction-side gill region film cooling is investigated using the University of Utah transonic wind tunnel and a simulated turbine vane in a two-dimensional cascade. The effects of film cooling hole orientation, shape, and number of rows, and their resulting effects on thermal film cooling characteristics,

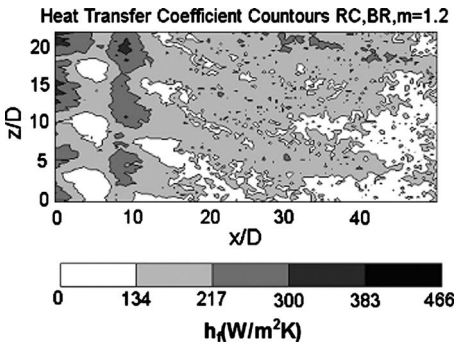

Fig. 14 Local film cooling heat transfer coefficient distribution for *m*=1.2 for the RC hole configuration and both rows of holes arrangement

are considered for four different hole configurations: RA, SA, RR, and RC. The mainstream Reynolds number based on axial chord is 500,000, the exit Mach number is 0.35, and the tests are conducted using the first row of holes only, second row of holes only, or both rows of holes at blowing ratios of 0.6 and 1.2. Carbon dioxide is used as the injectant to achieve density ratios of 1.73–1.92 similar to values present in operating gas turbine engines. A mesh grid is used to give a magnitude of longitudinal turbulence intensity of 5.7% at the inlet of the test section.

Results show that the best overall protection over the widest range of blowing ratios and streamwise locations is provided by either the RC holes or the RR holes. This result is particularly significant because the RR hole arrangement, which has lower manufacturing costs compared with the RC and SA arrangements, produces better or equivalent levels of performance in terms of magnitudes of adiabatic film cooling effectiveness and heat transfer coefficient. Such improved performance (relative to RA and SA holes) is likely mostly a result of compound angles, which increases lateral spreading. As such, the present results indicate that steep compound angle appears to be more effective than hole shaping in improving film cooling performance, increasing effectiveness values and providing superior spanwise injectant coverage. RR and RC configurations are thus a viable alternative to shaped holes in providing thermal protection on the suction-side gill region of a turbine vane, especially for the lower blowing ratios investigated.

Results also show that RA holes give the worst performance, with less coverage and lower effectiveness values compared with all the other hole configurations. The addition of hole shaping to the RA hole configurations gives the SA arrangement, which gives improved film cooling performance, both in terms of injectant coverage and effectiveness. This is especially for far downstream locations where $x/D > 40$. Adding compound angles to the RA configuration produces the RC configuration, which further increases effectiveness values and leads to further improvements in spanwise film coverage. Utilizing the RR configuration, in some cases, then gives equivalent or slightly improved film cooling performance relative to the RC arrangement. As such, the present study provides new data on film cooling performance for experimental conditions and configurations not previously investigated.

Acknowledgment

The authors gratefully acknowledge Pratt and Whitney Canada, who sponsored for this research effort. Dr. Qiang Zhang is also acknowledged for his guidance in regard to arrangement and operation of different test apparatus components.

Nomenclature

Bx = vane axial chord coordinate
c = specific heat
C = true vane chord length
C_x = axial chord length
d, D = film cooling hole entrance diameter
h_f = local film cooling heat transfer coefficient
$\overline{h}_f$ = spanwise-averaged film cooling heat transfer coefficient
k = molecular thermal conductivity
m = blowing ratio $(\rho_c u_c / \rho_\infty u_\infty)$
p = passage pitch
q_w = surface heat flux
t = time
T = temperature
u = local velocity
x = streamwise coordinate along vane surface measured from leading edge of first row of coolant holes
X = film cooling hole streamwise coordinate
Y = film cooling hole normal coordinate
z = spanwise coordinate along vane surface measured from spanwise centerline of the vane
Z = film cooling hole spanwise coordinate

Greek Symbols

α = molecular thermal diffusivity
η = local adiabatic film cooling effectiveness
$\overline{\eta}$ = spanwise-averaged adiabatic film cooling effectiveness
θ = film cooling holes inclination angle
ρ = local density

Subscripts

ad = adiabatic wall
c = injectant or film coolant value at exit planes of film cooling holes
i = initial value
∞ = local freestream value
o = total or stagnation value

References

[1] Goldstein, R. J., Eckert, E. R. G., and Burggraf, F., 1974, "Effects of Hole Geometry and Density on Three-Dimensional Film Cooling," Int. J. Heat Mass Transfer, **17**, pp. 595–607.
[2] Chen, P.-H., Ai, D., and Lee, S.-H., 1998, "Effects of Compound Angle Injection on Flat-Plate Film Cooling Through a Row of Conical Holes," ASME Paper No. 98-GT-459.
[3] Makki, Y. H., and Jakubowski, G. S., 1986, "An Experimental Study of Film Cooling From Diffused Trapezoid Shaped Holes," 24th Aerospace Sciences Meeting and Exhibit, Reno, NV, AIAA Paper No. 86-1326.
[4] Ajersch, P., Zhou, J.-M., Ketler, S., Salcudean, M., and Gartshore, I. S., 1995, "Multiple Jets in a Crossflow: Detailed Measurements and Numerical Simulations," ASME Paper No. 95-GT-9.
[5] Farmer, J. P., Seager, D. J., and Liburdy, J. A., 1997, "The Effect of Shaping Inclined Slots on Film Cooling Effectiveness and Heat Transfer Coefficient," ASME Paper No. 97-GT-339.
[6] Schmidt, D. L., Sen, B., and Bogard, D. G., 1996, "Film Cooling With Compound Angle Holes: Adiabatic Effectiveness," ASME J. Turbomach., **118**(4), pp. 807–813.
[7] Haven, B. A., and Kurosaka, M., 1996, "The Effect of Hole Geometry on Lift-Off Behavior of Coolant Jets," 34th Aerospace Sciences Meeting, and Exhibit, Reno, NV, AIAA Paper No. 96-0618.
[8] Hyams, D. G., and Leylek, J. H., 1997, "A Detailed Analysis of Film Cooling Physics, Part III: Streamwise Injection With Shaped Holes," ASME Paper No. 97-GT-271.
[9] Brittingham, R. A., and Leylek, J. H., 1997, "A Detailed Analysis of Film Cooling Physics, Part IV: Compound-Angle Injection With Shaped Holes," ASME Paper No. 97-GT-272.
[10] McGrath, E. L., and Leylek, J. H., 1998, "Physics of Hot Crossflow Ingestion in Film Cooling," ASME Paper No. 98-GT-191.
[11] Berger, P. A., and Liburdy, J. A., 1998, "A Near-Field Investigation Into the Effects of Geometry and Compound Angle on the Flowfield of a Row of Film Cooling Holes," ASME Paper No. 98-GT-279.
[12] Yu, Y., Yen, C.-H., Shih, T. I.-P., Chyu, M. K., and Gogineni, S., 1999, "Film Cooling Effectiveness and Heat Transfer Coefficient Distributions Around Diffusion Shaped Holes," ASME Paper No. 99-GT-34.
[13] Chen, P.-H., Ding, P.-P., Hung, M.-S., and Shih, P.-C., 1999, "Film Cooling Over a Concave Surface Through a Row of Expanded Holes," ASME Paper No. 99-GT-33.
[14] Bell, C. M., Hamakawa, H., and Ligrani, P. M., 2000, "Film Cooling From Shaped Holes," ASME J. Heat Transfer, **122**(2), pp. 224–232.
[15] Giebert, D., Gritsch, M., Schulz, A., and Wittig, S., 1997, "Film-Cooling From Holes With Expanded Exits: A Comparison of Computational Results With Experiments," ASME Paper No. 97-GT-163.
[16] Thole, K., Gritsch, M., Schulz, A., and Wittig, S., 1998, "Flowfield Measurements for Film-Cooling Holes With Expanded Exits," ASME J. Turbomach., **120**(2), pp. 327–336.
[17] Gritsch, M., Schulz, A., and Wittig, S., 1998, "Adiabatic Wall Effectiveness Measurements of Film-Cooling Holes With Expanded Exits," ASME J. Turbomach., **120**(3), pp. 549–556.
[18] Reiss, H., and Bolcs, A., 1999, "Experimental Study of Showerhead Cooling on a Cylinder Comparing Several Configurations Using Cylindrical and Shaped Holes," ASME Paper No. 99-GT-123.
[19] Teng, S., and Han, J. C., 2000, "Effect of Film-Hole Shape on Turbine Blade Heat Transfer Coefficient Distribution," 38th Aerospace Sciences Meeting, and Exhibit, Reno, NV, AIAA Paper No. AIAA 2000-1035.
[20] Kohli, A., and Thole, K. A., 1998, "Entrance Effects on Diffused Film Cooling Holes," ASME Paper No. 98-GT-402.
[21] Khole, A., and Bogard, D. G., 1999, "Effects of Hole Shape on Film Cooling With Large Angle Injection," ASME Paper No. 99-GT-165.
[22] Cho, H. H., Rhee, D. H., and Kim, B. G., 1999, "Film Cooling Effectiveness

and Heat/Mass Transfer Coefficient Measurement Around a Conical-Shaped Hole With a Compound Angle Injection," ASME Paper No. 99-GT-38.
[23] Brandt, H., Ganzert, W., and Fottner, L., 2000, "A Presentation of Detailed Experimental Data of a Suction Side Film Cooled Turbine Cascade," ASME Paper No. 2000-GT-296.
[24] Furukawa, T., and Ligrani, P. M., 2002, "Transonic Film Cooling Effectiveness From Shaped Holes on a Simulated Turbine Airfoil," J. Thermophys. Heat Transfer, **16**, pp. 228–237.
[25] Chappell, J., Ligrani, P. M., Sreekanth, S., Lucas, T., and E. Vlasic, 2008, "Aerodynamic Performance of Suction-Side Gill-Region Film Cooling," ASME Paper No. GT2008-50799.
[26] Zhang, Q., and Ligrani, P. M., 2004, "Mach Number/Surface Roughness Effects on Symmetric Transonic Turbine Airfoil Aerodynamic Losses," J. Propul. Power, **20**(6), pp. 1117–1125.
[27] Jackson, D. J., Lee, K. L., Ligrani, P. M., and Johnson, P. D., 2000, "Transonic Aerodynamics Losses Due to Turbine Airfoil, Suction Surface Film Cooling," ASME J. Turbomach., **122**, pp. 317–326.
[28] Zhang, Q., Sandberg, D., and Ligrani, P., 2005, "Influence of Mach Number and Freestream Turbulence Intensity on the Aerodynamic Losses of a Turbine Vane," J. Propul. Power, **21**(6), pp. 988–996.
[29] Carslaw, H. S., and Jaeger, J. C., 1959, *Conduction of Heat in Solids*, 2nd ed., Oxford University, New York.
[30] Metzger, D. E., and Larson, D. E., 1986, "Use of Melting Point Surface Coatings for Local Convection Heat Transfer Measurements in Rectangular Channel Flows With 90-Deg Turns," ASME J. Heat Transfer, **108**, pp. 48–54.
[31] Kline, S. J., and McClintock, F. A., 1953, "Describing Uncertainties in Single Sample Experiments," Mech. Eng. (Am. Soc. Mech. Eng.), **75**, pp. 3–8.
[32] Moffat, R. J., 1988, "Describing the Uncertainties in Experimental Results," Exp. Therm. Fluid Sci., **1**, pp. 3–17.